Article

Quantum spin nematic phase in a square-lattice iridate

https://doi.org/10.1038/s41586-023-06829-4

Received: 11 March 2023

Accepted: 3 November 2023

Published online: 13 December 2023

Check for updates

Hoon Kim[1,2,9], Jin-Kwang Kim[1,2,9], Junyoung Kwon[2], Jimin Kim[1,2], Hyun-Woo J. Kim[1,2], Seunghyeok Ha[1,2], Kwangrae Kim[1,2], Wonjun Lee[1,2], Jonghwan Kim[3,4], Gil Young Cho[1,2], Hyeokjun Heo[5], Joonho Jang[5], C. J. Sahle[6], A. Longo[6,7], J. Strempfer[8], G. Fabbris[8], Y. Choi[8], D. Haskel[8], Jungho Kim[8], J. -W. Kim[8] & B. J. Kim[1,2]✉

Spin nematic is a magnetic analogue of classical liquid crystals, a fourth state of matter exhibiting characteristics of both liquid and solid[1,2]. Particularly intriguing is a valence-bond spin nematic[3–5], in which spins are quantum entangled to form a multipolar order without breaking time-reversal symmetry, but its unambiguous experimental realization remains elusive. Here we establish a spin nematic phase in the square-lattice iridate Sr_2IrO_4, which approximately realizes a pseudospin one-half Heisenberg antiferromagnet in the strong spin–orbit coupling limit[6–9]. Upon cooling, the transition into the spin nematic phase at $T_C \approx 263$ K is marked by a divergence in the static spin quadrupole susceptibility extracted from our Raman spectra and concomitant emergence of a collective mode associated with the spontaneous breaking of rotational symmetries. The quadrupolar order persists in the antiferromagnetic phase below $T_N \approx 230$ K and becomes directly observable through its interference with the antiferromagnetic order in resonant X-ray diffraction, which allows us to uniquely determine its spatial structure. Further, we find using resonant inelastic X-ray scattering a complete breakdown of coherent magnon excitations at short-wavelength scales, suggesting a many-body quantum entanglement in the antiferromagnetic state[10,11]. Taken together, our results reveal a quantum order underlying the Néel antiferromagnet that is widely believed to be intimately connected to the mechanism of high-temperature superconductivity[12,13].

With its relevance to high-temperature superconductivity in cuprates, the spin one-half ($S = 1/2$) Heisenberg model on a square lattice has been a subject of extensive research over the last several decades[9,13,14]. Although the Mermin–Wagner theorem states that continuous symmetries cannot be spontaneously broken in two dimensions, it is well established that Néel-type antiferromagnetic orders develop at low temperatures because of weak interlayer couplings that form a three-dimensional network in quasi-two-dimensional materials[15]. Nevertheless, spins retain much of their properties in the disordered phase and undergo large quantum zero-point motions[16]. The resulting ground-state wave function is believed to embody a highly non-trivial structure akin to those in quantum spin liquids. For instance, the resonant valence bond, a superposition of states in which spins pair up to form singlet 'valence bonds', may have substantial overlap with the ground state[12] (Fig. 1). Upon carrier doping, these singlets evolve into Cooper pairs in a prominent theory of high-temperature superconductivity[12,13].

What is not well known, however, is the fact that such quantum entanglement between a pair of nearest-neighbour spins can also manifest as an ordered spin quadrupole moment when spins are canted[3–5] (Fig. 1). Because quadrupole moment can be non-zero only for $S \geq 1$, the existence of a quadrupolar order in an $S = 1/2$ system necessarily implies that spin pairs are entangled and have $S = 1$ triplet components. Unlike singlets, however, a quadrupolar order is, in principle, measurable[17,18] as it leads to spontaneous breaking of rotation symmetries[19,20]. In this article, we show that a quadrupolar order coexists with the Néel antiferromagnetic order in Sr_2IrO_4, a single-layer ($n = 1$) member of the Ruddlesden–Popper series iridates (Fig. 2a), which has received much attention because of similarities with superconducting cuprates in their phenomenology[6–9]. Furthermore, we show that it persists above T_N and realizes a spin nematic phase.

Resonant X-ray diffraction

We use resonant X-ray diffraction (RXD) to show the coexistence of a quadrupolar and dipolar (canted antiferromagnetic) order (Fig. 2a). The dipole–quadrupole interference contribution to the RXD intensity can be isolated by measuring the circular dichroic signal (I_{CD}) of a magnetic Bragg reflection defined as

[1]Center for Artificial Low Dimensional Electronic Systems, Institute for Basic Science, Pohang, South Korea. [2]Department of Physics, Pohang University of Science and Technology, Pohang, South Korea. [3]Center for Van der Waals Quantum Solids, Institute for Basic Science, Pohang, Korea. [4]Department of Materials Science and Engineering, Pohang University of Science and Technology, Pohang, Korea. [5]Department of Physics and Astronomy, Seoul National University, Seoul, South Korea. [6]ESRF, The European Synchrotron, Grenoble, France. [7]Istituto per lo Studio dei Materiali Nanostrutturati (ISMN)-CNR, UOS Palermo, Palermo, Italy. [8]Advanced Photon Source, Argonne National Laboratory, Argonne, IL, USA. [9]These authors contributed equally: Hoon Kim, Jin-Kwang Kim. ✉e-mail: bjkim6@postech.ac.kr

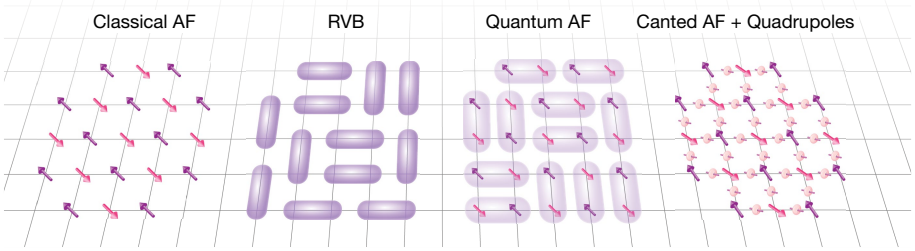

Fig. 1 | Spin one-half moments on a square lattice. In strict two dimensions, antiferromagnetic order is not allowed at any finite temperature, and spins are disordered but quantum entangled in a non-trivial way. For example, resonant valence bond (RVB) is a state in which spins pair up to form singlets and fluctuate among numerous different configurations covering the square lattice with such dimers. Although most quasi-two-dimensional materials develop antiferromagnetic orders because of weak interlayer couplings, spins still undergo strong quantum fluctuations. In a canted antiferromagnetic, quantum entanglement can manifest as an ordered spin quadrupole moment. AF, antiferromagnetic.

$$I_{CD}=\frac{I_{DIFF}}{I_{SUM}}=\frac{I_{LL}+I_{LR}-I_{RR}-I_{RL}}{I_{LL}+I_{LR}+I_{RR}+I_{RL}}, \quad (1)$$

where $I_{L(R)L(R)}$ denotes the intensity of left (right) circular polarized incident X-ray scattered into the left (right) circular outgoing X-ray. This definition of I_{CD} reflects the fact that the scattered X-ray polarization is not resolved in our experiment. It is straightforward to show that the difference spectrum (I_{DIFF}) in our particular case can be expressed as (Supplementary Note 1)

$$I_{DIFF}\propto F_1^M e_1^A F_2^Q e_2^S+F_1^Q e_1^S F_2^M e_2^A-F_2^M e_1^A F_1^Q e_2^S-F_2^Q e_1^S F_1^M e_2^A, \quad (2)$$

where $F_{1,2}^Q$ and $F_{1,2}^M$ couple to symmetric (e_1^S) and antisymmetric (e_2^A) components of the polarization tensor $e_{\alpha\beta}\equiv\epsilon'^*_\alpha\epsilon_\beta$, respectively, and represent the complex structure factor ($F\equiv F_1+iF_2$) associated with time-reversal-even quadrupoles and time-reversal-odd dipoles, respectively. Thus, circular dichroism arises from the interference between dipolar and quadrupolar scatterings in the electric–dipole–electric–dipole (*E*1–*E*1) process of RXD. In Supplementary Note 2, we argue that this is the unique explanation for the circular dichroic in our case among all known mechanisms.

Figure 2b,c shows the representative resonance profile of the (0 0 21) reflection, arising from the net ferromagnetic moment owing to canting of the spins[7], at two different azimuth angles (Ψ) defined as the angle between the crystallographic *a* axis and the vertical scattering plane. I_{DIFF} is non-zero at and close to the resonance and positive (negative) at $\Psi=30°$ ($\Psi=-56°$). Figure 2d,e shows the sum spectra (I_{SUM}) and I_{DIFF} at the resonance for the full range of Ψ measured. The Ψ dependence of I_{CD} (Fig. 2f) allows us to determine the spatial structure and symmetry of the quadrupolar order. To systematically find all symmetry-allowed $\mathbf{q}=0$ bond-centred quadrupole structures (Supplementary Note 3), we first note that the reflection appearing at (0 0 21) implies that both the dipolar and quadrupolar orders break the body-centre translation symmetry. Such structures are represented by one of the four irreducible representations Γ_1, Γ_2, Γ_3 and Γ_4, which are all two dimensional. For example, it is known that the magnetic structure shown in Fig. 2a belongs to Γ_1 irreducible representation[21].

Although there are many different possible quadrupole structures (Supplementary Note 3), there are only a few that have non-zero structure factors, which involve *yz*/*zx* quadrupoles for Γ_1 and Γ_2, *xy* for Γ_3 and $x^2-y^2/3z^2-r^2$ for Γ_4. In Fig. 2f, the Ψ dependence of I_{CD} is simulated for each of these structures and compared with the data. We find that only the Γ_1 structure, depicted in Fig. 2a, is consistent with the experimental data, the key feature of which is the sign change at $\Psi=0°$. The total scattering amplitude is given by

$$F=F^M+rF^Q=i\begin{pmatrix}0 & 0 & -cM_y\\ 0 & 0 & c^*M_x\\ cM_y & -c^*M_x & 0\end{pmatrix}+r\begin{pmatrix}0 & 0 & cQ_{zx}\\ 0 & 0 & c^*Q_{yz}\\ cQ_{zx} & c^*Q_{yz} & 0\end{pmatrix}, \quad (3)$$

where $\mathbf{M}=(M_x, M_y)$ and $\mathbf{Q}=(Q_{yz}, Q_{zx})$ are two-dimensional real basis vectors (whose transformation matrices are listed in Supplementary Note 3) for Γ_1 representing the net ferromagnetic component of the magnetic order and the quadrupolar order, respectively, normalized to one when they have the maximal values and $c=4(1-i)$ is a constant arising from the structure factor. *r* is a dimensionless factor accounting for the fact that quadrupoles only become visible by high-order RXD processes (Supplementary Note 4 has possible microscopic mechanisms).

For the magnetic order, it is known that the easy axis is along <100> (ref. 22), and the fact that I_{SUM} has a minimum at $\Psi=0°$ means that the magnetic domain being measured has the ferromagnetic (antiferromagnetic) component along the *b* (*a*) axis; hence, $M_x=0$. As we shall see below, fixing the direction of $\mathbf{M}$ along *y* constrains Q_{yz} to be zero. Thus, it follows that

$$I_{CD}=\frac{(rQ_{zx}/M_y)\ \sin\alpha\sin2\Psi}{1-\cos2\alpha\cos\Psi^2+(rQ_{zx}/M_y)^2\sin\Psi^2}, \quad (4)$$

where α is the incidence angle to the sample surface (approximately 27°). Thus, the data can be fit with rQ_{zx}/M_y as the only fitting parameter, and the best fit is obtained when $rQ_{zx}/M_y\approx0.04$ (Fig. 2f). With a quantitative estimate of the *r* factor, which is beyond the scope of this work, one can in principle compare the relative magnitudes of Q_{zx} and M_y.

Two-site $S=1/2$ model

When a quadrupolar order coexists with a dipolar order, its allowed structure is constrained by the orientation of the dipolar order. For example, for a single $S=1$ spin, it is easy to show that if its dipole moment is along *z*, then *yz* and *zx* quadrupole moments are zero. For the present case, we proceed with a simple two-site $S=1/2$ model (Supplementary Note 5). An arbitrary wave function for a pair of nearest-neighbour spins can be expressed in the singlet–triplet basis (s, T_x, T_y, T_z) in terms of two parameters θ and ϕ as $\mathbf{u}+i\mathbf{v}$, where

$$\begin{aligned}\mathbf{u}&=\cos\theta(\cos\phi\cos\phi_c, -\sin\phi,\ 0,\ \cos\phi\sin\phi_c),\\ \mathbf{v}&=\sin\theta\ (\sin\phi\cos\phi_c,\ \ \cos\phi,\ 0,\ \sin\phi\sin\phi_c),\end{aligned} \quad (5)$$

under the constraints that the antiferromagnetic (ferromagnetic) component of the ordered moment is along *a*(*b*) axis and the canting angle $\phi_c\approx12°$ (that is, $\langle N_y\rangle=\langle N_z\rangle=\langle M_x\rangle=\langle M_z\rangle=0$ and $\langle M_y\rangle/\langle N_x\rangle=\tan\phi_c$, where $N_\alpha\equiv S_\alpha^1-S_\alpha^2$ and $M_\alpha\equiv S_\alpha^1+S_\alpha^2$).

Table 1 compares the magnitudes of magnetic and non-magnetic orders calculated as functions of θ and ϕ. First, we find that $\langle Q_{xy}\rangle=\langle Q_{yz}\rangle=0$ for all values of θ and ϕ, but $\langle Q_{zx}\rangle$ can be non-zero only when ϕ_c is non-zero. This suggests that the Dzyloshinskii–Moriya interaction plays an important role in stabilizing the quadrupolar order because the spin canting arises from the same origin[8]. Second, it is clear that θ parameterizes the competition between the magnetic

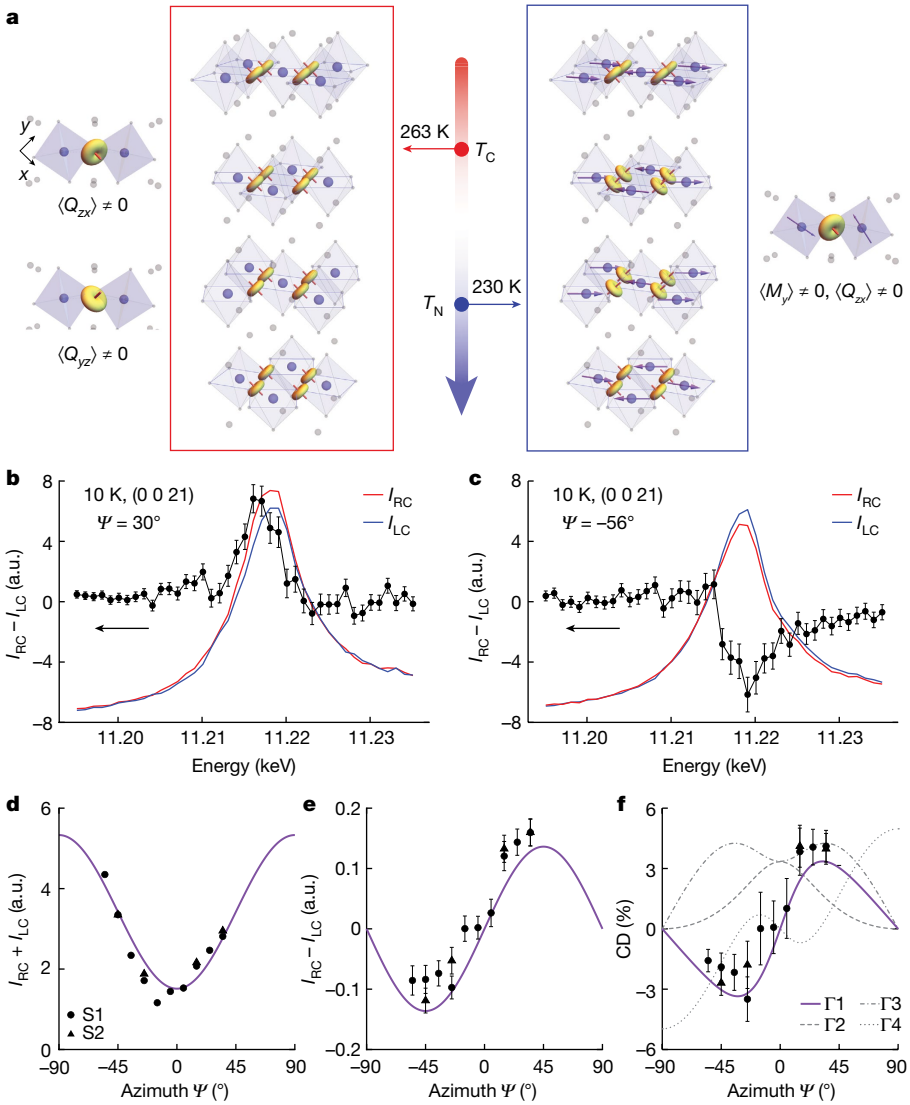

Fig. 2 | Dipole–quadrupole interference in circular dichroic RXD. **a**, A schematic for the Néel and spin nematic orders overlaid on the crystal structure of Sr_2IrO_4 having the tetragonal $I4_1/acd$ space group. The magnetic and quadrupole moments mutually constrain their orientations below the Néel temperature T_N (right panel), whereas (Q_{zx}, Q_{yz}) transforms as an E_g doublet above T_N (left panel). **b**,**c**, Resonance profile of the circular dichroic signal at (0 0 21) magnetic reflection measured at $\Psi = 30°$ (**b**) and $\Psi = -56°$ (**c**). I_{RC} (red) and I_{LC} (blue) denote the diffraction intensity for right- and left-circularly polarized incident X-rays, respectively. **d**,**e**, $I_{SUM} \equiv I_{RC} + I_{LC}$ (**d**) and $I_{DIFF} \equiv I_{RC} - I_{LC}$ (**e**) at the resonance for the full range of Ψ measured. S1 and S2 are obtained from two independent measurements. **f**, Comparison of $I_{CD} \equiv I_{DIFF}/I_{SUM}$ with the simulations for different irreducible representations. The best fit to the data using the Γ_1 profile is shown in **d**–**f**, and its structure is shown in **a**. Error bars represent one standard deviation. a.u., arbitrary unit; CD, circular dichroic.

and non-magnetic sectors. For example, at $\theta = \frac{\pi}{4}$, the magnetic moment fully saturates and $\langle Q_{zx}\rangle = 0$. Third, in the non-magnetic sector, ϕ controls the magnitude of $\langle Q_{zx}\rangle$, which anti-correlates with that of the dimer correlation $\langle -\mathbf{S}^1 \cdot \mathbf{S}^2 - \frac{1}{4}\rangle$, which takes the values $\frac{1}{2}$, 0 and $-\frac{1}{2}$ for the singlet, Néel antiferromagnetic state and triplets, respectively. In other words, just as the net ferromagnetic moment has its origin in the canting of antiferromagnetic spins, $\langle Q_{zx}\rangle$ arises from the underlying singlet correlation by 'canting' in angle ϕ.

Raman spectroscopy

Next, we use Raman spectroscopy, which has been suggested as a sensitive probe for spin nematic, to show that the quadrupolar order persists above T_N, armed with the information that the order should appear in the YZ or ZX polarization channel, which corresponds to the E_g symmetry channel of the tetragonal D_{4h} point group. This requires the laser beam to be incident on the side surface of a thin plate-like crystal, and thus, it has not been measured in previous Raman studies on Sr_2IrO_4 (refs. 23–25). Figure 3a shows the Raman spectra measured in ZX scattering geometry. Upon cooling down from $T = 325$ K, we observe a broad quasielastic feature developing with its tail extending up to less than or approximately 10 meV, which is indicative of slow fluctuations of spins (Fig. 3a). Integrating the Raman conductivity χ''/ω over a sufficiently

Table 1 | Quadrupole and dipole moments from the two-site S=1/2 model calculation

Type	Order	Expression
Antiferromagnetic	$\langle N_x\rangle$	$\sin2\theta\cos\phi_c$
Ferromagnetic	$\langle M_y\rangle$	$\sin2\theta\sin\phi_c$
Quadrupole	$\langle Q_{zx}\rangle$	$\frac{1}{2}(\cos2\theta\ \sin2\phi\ \sin\phi_c)$
Singlet	$\langle -\mathbf{S}^1 \cdot \mathbf{S}^2 - \frac{1}{4}\rangle$	$\frac{1}{2}(\cos2\theta\ \cos2\phi\ \cos^2\phi_c - \sin^2\phi_c)$

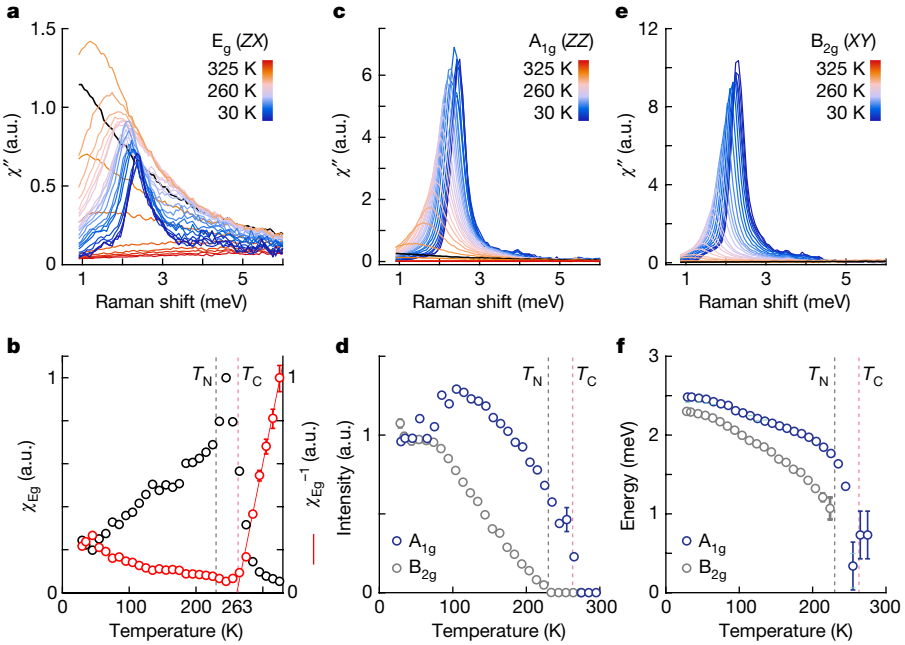

Fig. 3 | Phase transition into the spin nematic phase. a, Raman spectra in the E_g symmetry channel measured on cooling. **b**, The real part of the uniform static susceptibility (black) obtained by integrating the E_g Raman conductivity χ''/ω. The inverse susceptibility (red) exhibits a Curie–Weiss behaviour with $T_C \simeq 263$ K. The error bars represent the statistical uncertainty in the intensities assuming Poisson counting statistics. **c**,**e**, A_{1g} phase mode emerges at T_C (**c**), and the B_{2g} magnon emerges below T_N (**e**). **d**,**f**, Temperature dependence of the intensities (**d**) and energies (**f**) of A_{1g} and B_{2g} modes extracted by fitting the spectra to Fano profiles $I(\omega) = \frac{I_0}{\Gamma(1-q^2)}\left(1-\frac{(q+\epsilon)^2}{1+\epsilon^2}\right)$, where $\epsilon = (\omega-\omega_0)/\Gamma$, Γ is the linewidth and q is the asymmetry parameter. The error bars are the standard deviation from the least squares fitting. The intensity curves in **d** are normalized by the low-temperature values.

large energy window (0.85–23.4 meV), we obtain in Fig. 3b the real part of the static susceptibility, which follows the Curie–Weiss temperature dependence with $T_C \approx 263$ K.

Concomitantly, an A_{1g} mode emerges (Fig. 3c and Extended Data Fig. 1), which is barely visible above our instrumental low-energy cutoff of approximately 0.85 meV at T_C but upon further cooling, becomes well resolved as the peak moves to higher energies. We interpret this peak as the phase mode associated with the quadrupolar order, analogous to spin-wave modes in the antiferromagnetic phase. The order parameter has E_g symmetry, which can be continuously rotated about the c axis. This allows the phase mode to have the energy (1–2 meV), an order of magnitude smaller than the temperature scale of T_C (approximately 20 meV), in accordance with the Goldstone theorem. Together with the divergence in the static susceptibility, this collective excitation constitutes direct evidence of a thermodynamic phase transition at $T_C \approx 263$ K, well above the antiferromagnetic transition temperature $T_N \approx 230$ K.

The A_{1g} mode persists as the sample is cooled down through T_N (Fig. 3c,d), at which temperature the B_{2g} single-magnon mode emerges (Fig. 3e). The A_{1g} mode becomes gapped close to T_N as the antiferromagnetic order further reinforces the breaking of the rotational symmetry (Fig. 3f). The intensity of the A_{1g} mode continues to grow in the antiferromagnetic phase (Fig. 3d), implying the coexistence of dipolar and quadrupolar orders. As the antiferromagnetic order sets in, however, the stacking pattern of the quadrupoles changes, which is governed by weak interlayer interactions of less than or approximately 10 μeV energy scales, four orders of magnitudes smaller than those for intralayer interactions[22] (Fig. 2a). We note that the A_{1g} mode is almost insensitive to the onset of the dipolar order, indicating that spins entanglement remains intact below T_N.

Resonant inelastic X-ray scattering

If the quadrupolar order comprises a substantial part of the ground state (small θ limit in equation (5)), excitation spectra must exhibit a qualitative departure from the classical spin-wave theory, which largely reproduces the experimental spectra of cuprate square-lattice antiferromagnets[26]. Figure 4 shows the resonant inelastic X-ray scattering (RIXS) spectra for the spin components transverse and longitudinal to the ordered moment direction, which we resolve by measuring the spectra for two different magnetic moment directions aligned using a small permanent magnet (Extended Data Table 1 and Supplementary Note 6). At the ordering wave vector (π, π) (Fig. 4b), the spectral weight is mostly in the transverse channel, consistent with the spin-wave theory description, which expects a divergent intensity for a gapless Goldstone mode. The transverse magnon mode is also clearly visible at (π/2, π/2), although a considerable weight is transferred to the longitudinal channel (Fig. 4c). By contrast, at (π, 0) the spectrum is completely isotropic and shows no sharp feature that can be identified as a magnon mode (Fig. 4d). We note that the zone-boundary RIXS spectra are hardly affected by the small magnetic field (Supplementary Note 6).

In the cuprates, the '(π, 0) anomaly' is ubiquitously observed across many different materials[10,27–30], and from its isotropic nature, the continuum has been interpreted as deconfined fractional quasiparticles (spinons)[10,11]. We note, however, that the transverse mode still constitutes the dominant part of the total intensity in most cases. To the best of our knowledge, the complete loss of the coherent magnon intensity is unprecedented and renders alternative multimagnon scenarios[31] unlikely in our case.

Discussion

Theoretically, spin nematics are predicted to arise in certain spin models with competing interactions[1,32–37]. For example, in a square lattice, four-spin exchange (J_c) competing with ferromagnetic nearest-neighbour Heisenberg exchange (J) can lead to a spin nematic[2,4,5]. In this regard, 5*d* transition-metal oxides, classified as 'weak' Mott insulators stabilized by strong spin-orbit coupling, may be a promising ground to search for a spin nematic because the large spatial extent

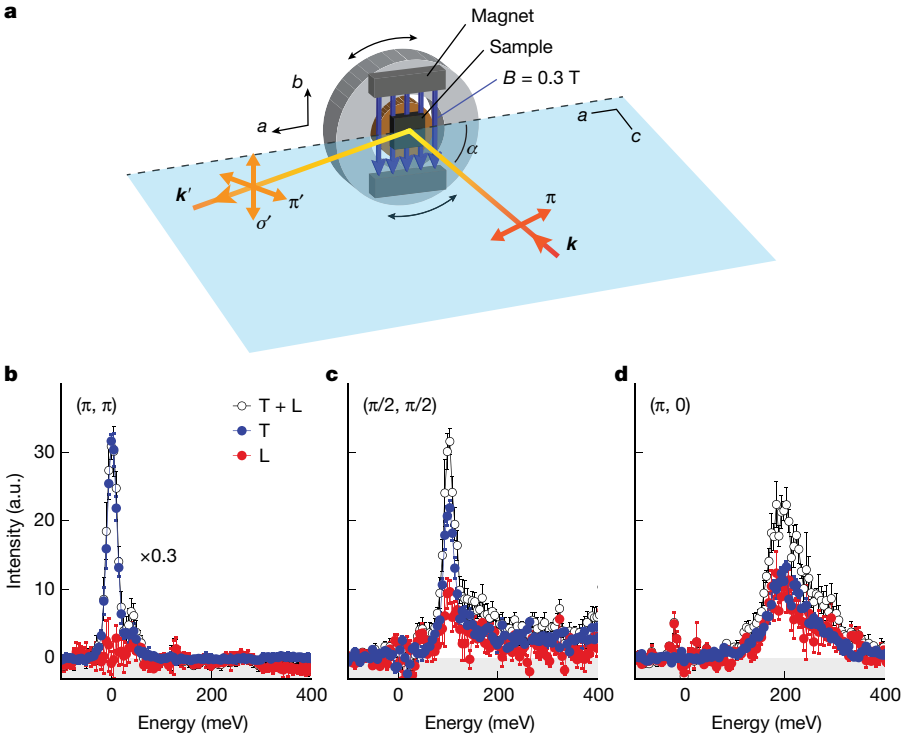

Fig. 4 | Complete breakdown of magnon at short-wavelength scales. **a**, A schematic of the RIXS geometry. X-rays with π polarization are incident to the sample with the angle $\alpha \approx 75°$, and scattered X-rays are collected without polarization analysis. A single crystal of Sr_2IrO_4 is placed between two permanent magnets that apply a magnetic field of 0.3 T along the *b* axis (*a* axis) at the sample position aligning the magnetic domains (that is, $\mathbf{M} \| \hat{b}$ ($\mathbf{M} \| \hat{a}$)). The direction of the applied field can be changed by rotating the outer disk on which the magnets are mounted while the sample stays fixed. The angle between the incident and outgoing X-rays is fixed close to 90° to suppress elastic Thomson scattering. **b**–**d**, RIXS spectra for (π, π) (**b**), (π/2, π/2) (**c**) and (π, 0) (**d**). The transverse (T) mode and the longitudinal (L) mode are displayed along with the sum of the two (T + L). Solid lines are guides to the eye. The components are extracted from the raw spectra measured in different magnetic field directions with a fixed scattering geometry (Extended Data Table 1 and Supplementary Note 6). The spectra measured at intermediate wavevectors between (π/2, π/2) and (π, 0) are displayed in Extended Data Fig. 3. Error bars are determined using error propagation of the intensity uncertainties in the raw spectra.

of the 5*d* orbitals can bring about strong competing interactions with nearest-neighbour Heisenberg interactions[9]. Indeed, the presence of interaction terms beyond nearest neighbour in Sr_2IrO_4 is clear from its steep spin-wave dispersion along the magnetic zone boundary[38], which can be equally well fitted with a model including J_c or further-neighbour couplings (J_2 and J_3). Further, our study suggests that the large canting angle of the spins resulting in a sizable net ferromagnetic moment in each layer may be favourable for stabilizing the spin nematic phase even in an Néel antiferromagnet.

The fact that *L* edges of 5*d* transition-metal elements are in the hard X-ray regime with access to a wide region in the momentum space is also advantageous for direct detection of spin quadrupoles, as X-rays become sensitive to quadrupoles under resonance conditions[17,18]. Most other experimental probes are insensitive to spin quadrupoles, and evidence for a spin nematic has so far been indirectly provided from thermodynamic[19,39] and nuclear magnetic resonance measurements[20]. In Sr_2IrO_4, evidence for a symmetry-breaking order above T_N has been found in studies using second harmonic generation[40], polarized neutron scattering[41] and magnetic torque measurements[42]. These studies suggest loop currents as the possible order. Although our result is inconsistent with such a time-reversal symmetry-breaking order (Extended Data Fig. 2), it is possible that these experiments are probing yet another order of different nature (Extended Data Table 2).

Our results vividly demonstrate that multiple orders are intertwined even in the Mott insulating phase. The discovery of the spin nematic phase is not only important on its own, but it also paves a new pathway to investigate the entanglement structure of quantum spins through resonant X-ray scattering processes[18]. The quantum entanglement between nearest-neighbour spins manifests as a spin quadrupolar order and possibly accounts for the complete loss of coherent magnons at momentum (π, 0). If quadrupolar orders can be detected through charge–quadrupole interference, their temperature and doping evolution can be followed in the absence of a magnetic order, with the ultimate goal of elucidating the role of magnetic correlations in myriad exotic phases displayed by doped Mott insulators.

Online content

Any methods, additional references, Nature Portfolio reporting summaries, source data, extended data, supplementary information, acknowledgements, peer review information; details of author contributions and competing interests; and statements of data and code availability are available at https://doi.org/10.1038/s41586-023-06829-4.

1. Blume, M. & Hsieh, Y. Y. Biquadratic exchange and quadrupolar ordering. *J. Appl. Phys.* **40**, 1249–1249 (1969).
2. Andreev, A. F. & Grishchuk, I. A. Spin nematics. *Sov. Phys. JETP* **60**, 267–271 (1984).
3. Läuchli, A., Domenge, J. C., Lhuillier, C., Sindzingre, P. & Troyer, M. Two-step restoration of SU(2) symmetry in a frustrated ring-exchange magnet. *Phys. Rev. Lett.* **95**, 137206 (2005).
4. Shannon, N., Momoi, T. & Sindzingre, P. Nematic order in square lattice frustrated ferromagnets. *Phys. Rev. Lett.* **96**, 027213 (2006).
5. Sato, M., Hikihara, T. & Momoi, T. Spin-nematic and spin-density-wave orders in spatially anisotropic frustrated magnets in a magnetic field. *Phys. Rev. Lett.* **110**, 077206 (2013).
6. Kim, B. J. et al. Novel J_{eff}=1/2 Mott state induced by relativistic spin-orbit coupling in Sr_2IrO_4. *Phys. Rev. Lett.* **101**, 076402 (2008).
7. Kim, B. J. et al. Phase-sensitive observation of a spin-orbital mott state in Sr_2IrO_4. *Science* **323**, 1329–1332 (2009).
8. Jackeli, G. & Khaliullin, G. Mott insulators in the strong spin-orbit coupling limit: from Heisenberg to a quantum compass and Kitaev models. *Phys. Rev. Lett.* **102**, 017205 (2009).

9. Bertinshaw, J., Kim, Y. K., Khaliullin, G. & Kim, B. J. Square lattice iridates. *Annu. Rev. Condens. Matter Phys.* **10**, 315–336 (2019).
10. Dalla Piazza, B. et al. Fractional excitations in the square-lattice quantum antiferromagnet. *Nat. Phys.* **11**, 62–68 (2015).
11. Shao, H. et al. Nearly deconfined spinon excitations in the square-lattice spin-1/2 Heisenberg antiferromagnet. *Phys. Rev. X* **7**, 041072 (2017).
12. Anderson, P. W. The resonating valence bond state in La_2CuO_4 and superconductivity. *Science* **235**, 1196–1198 (1987).
13. Lee, P. A., Nagaosa, N. & Wen, X.-G. Doping a Mott insulator: physics of high-temperature superconductivity. *Rev. Mod. Phys.* **78**, 17–85 (2006).
14. Scalapino, D. J. A common thread: the pairing interaction for unconventional superconductors. *Rev. Mod. Phys.* **84**, 1383–1417 (2012).
15. Vaknin, D. et al. Antiferromagnetism in La_2CuO_{4-y}. *Phys. Rev. Lett.* **58**, 2802–2805 (1987).
16. Singh, R. R. P. Thermodynamic parameters of the $T=0$, spin-1/2 square-lattice Heisenberg antiferromagnet. *Phys. Rev. B* **39**, 9760–9763 (1989).
17. Smerald, A. & Shannon, N. Theory of spin excitations in a quantum spin-nematic state. *Phys. Rev. B* **88**, 184430 (2013).
18. Savary, L. & Senthil, T. Probing hidden orders with resonant inelastic X-ray scattering. Preprint at arxiv.org/abs/1506.04752 (2015).
19. Kohama, Y. et al. Possible observation of quantum spin-nematic phase in a frustrated magnet. *Proc. Natl Acad. Sci. USA* **116**, 10686–10690 (2019).
20. Orlova, A. et al. Nuclear magnetic resonance signature of the spin-nematic phase in $LiCuVO_4$ at high magnetic fields. *Phys. Rev. Lett.* **118**, 247201 (2017).
21. Ye, F. et al. Magnetic and crystal structures of Sr_2IrO_4: a neutron diffraction study. *Phys. Rev. B* **87**, 140406 (2013).
22. Porras, J. et al. Pseudospin-lattice coupling in the spin-orbit Mott insulator Sr_2IrO_4. *Phys. Rev. B* **99**, 085125 (2019).
23. Cetin, M. F. et al. Crossover from coherent to incoherent scattering in spin-orbit dominated Sr_2IrO_4. *Phys. Rev. B* **85**, 195148 (2012).
24. Gim, Y. et al. Isotropic and anisotropic regimes of the field-dependent spin dynamics in Sr_2IrO_4: Raman scattering studies. *Phys. Rev. B* **93**, 024405 (2016).
25. Gretarsson, H. et al. Two-magnon Raman scattering and pseudospin-lattice interactions in Sr_2IrO_4 and $Sr_3Ir_2O_7$. *Phys. Rev. Lett.* **116**, 136401 (2016).
26. Aeppli, G. et al. Magnetic dynamics of La_2CuO_4 and $La_{2-x}Ba_xCuO_4$. *Phys. Rev. Lett.* **62**, 2052–2055 (1989).
27. Christensen, N. B. et al. Quantum dynamics and entanglement of spins on a square lattice. *Proc. Natl Acad. Sci. USA* **104**, 15264–15269 (2007).
28. Headings, N. S., Hayden, S. M., Coldea, R. & Perring, T. G. Anomalous high-energy spin excitations in the high-T_c superconductor-parent antiferromagnet La_2CuO_4. *Phys. Rev. Lett.* **105**, 247001 (2010).
29. Martinelli, L. et al. Fractional spin excitations in the infinite-layer cuprate $CaCuO_2$. *Phys. Rev. X* **12**, 021041 (2022).
30. Tsyrulin, N. et al. Quantum effects in a weakly frustrated $S=1/2$ two-dimensional Heisenberg antiferromagnet in an applied magnetic field. *Phys. Rev. Lett.* **102**, 197201 (2009).
31. Powalski, M., Schmidt, K. P. & Uhrig, G. S. Mutually attracting spin waves in the square-lattice quantum antiferromagnet. *SciPost Phys.* **4**, 001 (2018).
32. Chen, H. H. & Levy, P. M. Quadrupole phase transitions in magnetic solids. *Phys. Rev. Lett.* **27**, 1383–1385 (1971).
33. Chandra, P. & Coleman, P. Quantum spin nematics: moment-free magnetism. *Phys. Rev. Lett.* **66**, 100–103 (1991).
34. Läuchli, A., Mila, F. & Penc, K. Quadrupolar phases of the $S=1$ bilinear-biquadratic Heisenberg model on the triangular lattice. *Phys. Rev. Lett.* **97**, 087205 (2006).
35. Hikihara, T., Kecke, L., Momoi, T. & Furusaki, A. Vector chiral and multipolar orders in the spin-$\frac{1}{2}$ frustrated ferromagnetic chain in magnetic field. *Phys. Rev. B* **78**, 144404 (2008).
36. Ueda, H. T. & Totsuka, K. Magnon bose-einstein condensation and various phases of three-dimensonal quantum helimagnets under high magnetic field. *Phys. Rev. B* **80**, 014417 (2009).
37. Zhitomirsky, M. E. & Tsunetsugu, H. Magnon pairing in quantum spin nematic. *EPL* **92**, 37001 (2010).
38. Kim, J. et al. Magnetic excitation spectra of Sr_2IrO_4 probed by resonant inelastic X-ray scattering: establishing links to cuprate superconductors. *Phys. Rev. Lett.* **108**, 177003 (2012).
39. Mourigal, M. et al. Evidence of a bond-nematic phase in $LiCuVO_4$. *Phys. Rev. Lett.* **109**, 027203 (2012).
40. Seyler, K. L. et al. Spin-orbit-enhanced magnetic surface second-harmonic generation in Sr_2IrO_4. *Phys. Rev. B* **102**, 201113 (2020).
41. Jeong, J., Sidis, Y., Louat, A., Brouet, V. & Bourges, P. Time-reversal symmetry breaking hidden order in $Sr_2(Ir,Rh)O_4$. *Nat. Commun.* **8**, 15119 (2017).
42. Murayama, H. et al. Bond directional anapole order in a spin-orbit coupled Mott insulator $Sr_2(Ir_{1-x}Rh_x)O_4$. *Phys. Rev. X* **11**, 011021 (2021).

Publisher's note Springer Nature remains neutral with regard to jurisdictional claims in published maps and institutional affiliations.

Springer Nature or its licensor (e.g. a society or other partner) holds exclusive rights to this article under a publishing agreement with the author(s) or other rightsholder(s); author self-archiving of the accepted manuscript version of this article is solely governed by the terms of such publishing agreement and applicable law.

© The Author(s), under exclusive licence to Springer Nature Limited 2023

Methods

Crystal growth

Single crystals of Sr_2IrO_4 were grown by the standard flux growth method. Powders of IrO_2, $SrCO_3$ and $SrCl_2{\cdot}6H_2O$ were mixed and placed in an iridium crucible covered with a lid. The mixture was melted and soaked at T = 1,300 °C, slowly cooled down to 900 °C at 8 °C per 1 h and then, furnace cooled to room temperature. We note that our crystals grown in an iridium crucible have the lattice structure of space group $I4_1/acd$ (ref. 43) and show no sign of the glide symmetry-breaking distortions previously reported[44].

RXD

RXD experiments were carried out at the 1C beamline of Pohang Accelerator Laboratory and the 4-ID-D beamline of the Advanced Photon Source. Incident X-ray was tuned at the Ir L_3 edge (11.217 keV). The focused beam having spatial resolution better than approximately 100 μm was used. The sample was mounted on the cold finger of a closed-cycle cryostat, and temperature was kept at 10 K throughout the experiment. The left and right circular polarized X-ray was generated using a diamond phase retarder. The helicity was switched at every data point to measure the flipping ratio of the circular dichroic signal.

RIXS

RIXS spectra were measured at the 27-ID-B beamline of the Advanced Photon Source and the ID20 beamline of the European Synchrotron Radiation Facility. Incident X-ray was tuned to the Ir L_3 edge (11.215 keV). Using a diamond (1 1 1) high-heat load monochromator in combination with an Si (8 4 4) channel-cut monochromator reduced the energy bandpass down to 14.8 meV. The beam was then focused by a set of Kirkpatrick–Baez mirrors, producing a spot size of 40 × 10 ($H \times V$) μm^2 full-width at half-maximum at the sample position. Scattered photons were analysed by an Si (8 4 4) diced spherical analyser with a radius of 2 m and with a mask of 2 inches in diameter for measurement at (π, π) and 3 inches for other momenta. The overall energy resolution was about 30 meV. A horizontal scattering geometry was used with the incident π polarization, and the outgoing polarization was not resolved. All RIXS spectra were taken around (3 0 28.5) in a normal incident scattering geometry, and a small magnetic field (approximately 0.3 T) was applied along either the a or b axis to align magnetic moments. The scattering angle (2θ) was kept around 90° to suppress elastic Thomson scatterings.

Raman spectroscopy

Raman spectroscopy was performed with a home-built setup equipped with a 633 nm He–Ne laser and a liquid nitrogen-cooled charge-coupled device (Princeton instruments). The elastic signal is removed by grating-based notch filters (Optigrate, BragGrate Notch filters). The spectra were acquired on as-grown surfaces of Sr_2IrO_4 crystals mounted in a closed-cycle optical cryostat (Montana instruments). The laser power and beam spot size are 0.8 mW and 2 μm, respectively, which resulted in an almost temperature-independent laser heating of 25 K as determined from the Stokes to anti-Stokes intensity ratio. All Raman spectra are Bose corrected.

Magneto-optical Kerr measurement

We performed magneto-optical Kerr measurements on Sr_2IrO_4 using an oblique-incidence zero-area Sagnac interferometer operating at 1,550 nm wavelength to measure the in-plane magnetization[45]. The relative Kerr angle $\Delta\theta_K$ is obtained by subtracting temperature-independent backgrounds, coming from the instrumentation offset, measured at T = 300 K and converted to magnetization (in μ_B per ion) by a quantitative comparison of our 0.35 T Kerr data with the corresponding magnetization data in ref. 22. Throughout the measurements, the incident optical power was maintained below 1 mW so that the effect of optical heating was smaller than 1 K.

Data availability

All data are available in the manuscript or Supplementary Information.

43. Kim, J. et al. Single crystal growth of iridates without platinum impurities. *Phys. Rev. Mater.* **6**, 103401 (2022).
44. Torchinsky, D. et al. Structural distortion-induced magnetoelastic locking in Sr_2IrO_4 revealed through nonlinear optical harmonic generation. *Phys. Rev. Lett.* **114**, 096404 (2015).
45. Zhu, X. D., Ullah, R. & Taufour, V. Oblique-incidence Sagnac interferometric scanning microscope for studying magneto-optic effects of materials at low temperatures. *Rev. Sci. Instrum.* **92**, 043706 (2021).
46. Varma, C. M. Non-Fermi-liquid states and pairing instability of a general model of copper oxide metals. *Phys. Rev. B* **55**, 14554–14580 (1997).
47. Zhao, L. et al. Evidence of an odd-parity hidden order in a spin-orbit coupled correlated iridate. *Nat. Phys.* **12**, 32–36 (2016).

Acknowledgements We thank N. Shannon, G. Khaliullin and Y. B. Kim for helpful discussions. This project is supported by the Institute for Basic Science (Project IBS-R014-A2) and the Samsung Science and Technology Foundation (Project SSTF-BA2201-04). Experiments at the PLS-II 1C beamline were supported in part by the Ministry of Science and ICT of Korea. The use of the Advanced Photon Source at the Argonne National Laboratory was supported by the US Department of Energy (Contract DE-AC02-06CH11357). We acknowledge the European Synchrotron Radiation Facility for provision of synchrotron radiation facilities (Proposal HC-5311), and we also thank F. Gerbon for assistance and support in using beamline ID20. J.-K.K. was supported by the Global PhD Fellowship Program by the National Research Foundation of Korea (Grant 2018H1A2A1059958). G.Y.C. is supported by the National Research Foundation of Korea (Grants 2020R1C1C1006048, RS-2023-00208291, 2023M3K5A1094810 and 2023M3K5A1094813) funded by the Korean Government (Ministry of Science and ICT), the Institute of Basic Science (Project IBS-R014-D1), the Air Force Office of Scientific Research (Award FA2386-22-1-4061) and the Samsung Science and Technology Foundation (Project SSTF-BA2002-05). H.H. and J.J. are supported by the National Research Foundation of Korea (Grant 2020R1A5A1016518) and the Creative-Pioneering Researchers Program through Seoul National University.

Author contributions B.J.K. conceived and managed the project. H.K., K.K. and Jonghwan Kim performed Raman experiments. H.K., J. Kwon and S.H. performed resonant X-ray diffraction experiments with help from J.S., G.F., Y.C., D.H. and J.W.K.; H.K., J.-K.K., J. Kwon and H.-W.J.K. performed resonant inelastic X-ray scattering experiments and analysed the data with help from C.J.S., A.L. and Jungho Kim. Jimin Kim grew single crystals. H.H. and J.J. performed Kerr measurements. H.K. and B.J.K. performed representation analysis. W.L. and G.Y.C. assisted in the interpretation of the data. H.K., J.-K.K. and B.J.K. wrote the manuscript with inputs from all authors.

Competing interests The authors declare no competing interests.

Additional information

Supplementary information The online version contains supplementary material available at https://doi.org/10.1038/s41586-023-06829-4.

Correspondence and requests for materials should be addressed to B. J. Kim.

Peer review information *Nature* thanks the anonymous reviewers for their contribution to the peer review of this work. Peer reviewer reports are available.

Reprints and permissions information is available at http://www.nature.com/reprints.

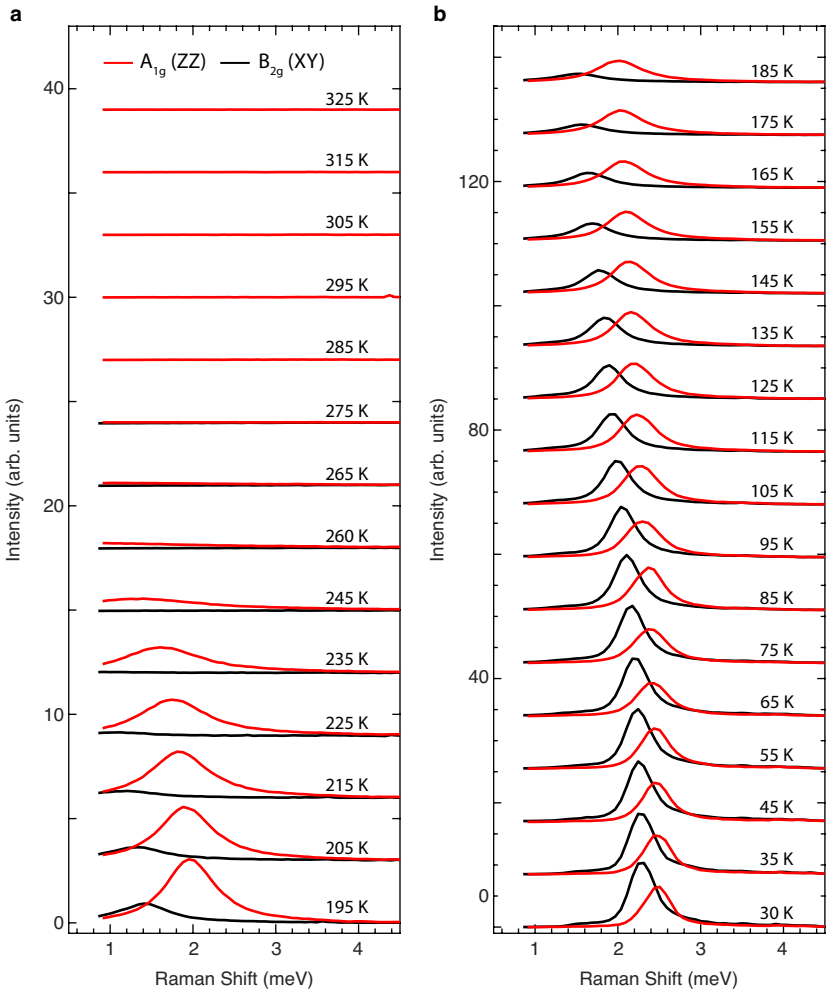

Extended Data Fig. 1 | Temperature evolution of the low-energy Raman modes. The Raman spectra of the A_{1g} and B_{2g} modes shown in Fig. 2c,e are displayed with vertical offset for clarity. The A_{1g} (red) and B_{2g} (black) spectra were measured on the same crystal under the same experimental conditions including laser power and acquisition time, and the spectra are plotted in the same arbitrary unit.

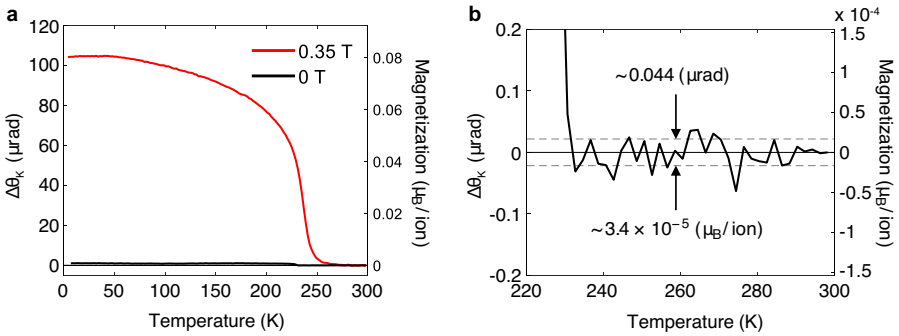

Extended Data Fig. 2 | Magneto-optical Kerr measurement. a, Relative Kerr angle in the 0.35 T in-plane magnetic field (red line) and ambient magnetic field near 0 T (black line). The relative Kerr angle (left axis) is converted to magnetization (right axis) using a conversion factor of 7.7×10^{-4} (μ_B/Ir ion)/(μrad). **b**, Magnified plot of the 0 T data in **a**. Dashed line indicates the standard deviation for the T = 230 ~ 300 K range. The Kerr signal at B = 0 T in the range of 230 K < T < 300 K shows that no net magnetization is present within our experimental resolution, 3.4×10^{-5} μ_B/ion (dashed line), thus confirming the preservation of time-reversal symmetry above T_N ~ 230 K.

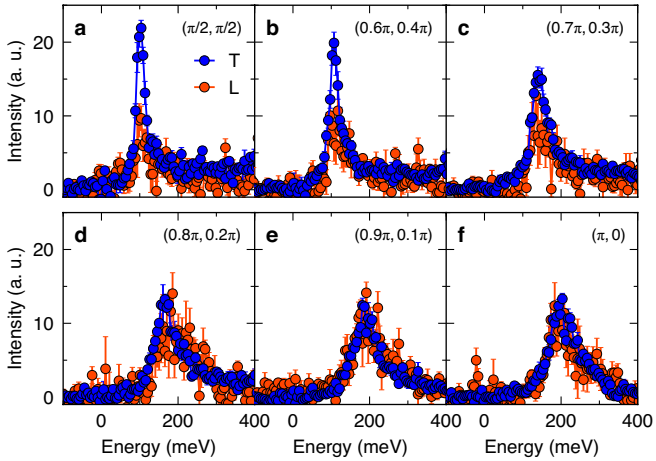

Extended Data Fig. 3 | Polarziation-resolved RIXS spectra. a–f, RIXS spectra along the zone boundary from ($\pi/2$, $\pi/2$) to (π, 0) with the spin components transverse (T) and longitudinal (L) to the ordered AF moments resolved. The spectra were acquired with the same experimental setup in Fig. 4. The error bars are derived using error propagation based on the standard deviations of the raw spectra.

Extended Data Table 1 | Sensitive mode for each combination of specific scattering geometry and field direction in RIXS measurements on Sr_2IrO_4

Incident angle	Field direction	Moment direction	Polarization	Sensitive element	Mode
Normal	[100]	[010]	$e_\pi \times e_{\pi'}$	[010]	L
			$e_\pi \times e_{\sigma'}$	[001]	T′
	[010]	[100]	$e_\pi \times e_{\pi'}$	[010]	T
			$e_\pi \times e_{\sigma'}$	[001]	T′
Grazing	[100]	[010]	$e_\pi \times e_{\pi'}$	[010]	L
			$e_\pi \times e_{\sigma'}$	[100]	T
	[010]	[100]	$e_\pi \times e_{\pi'}$	[010]	T
			$e_\pi \times e_{\sigma'}$	[100]	L

Here, L stands for the longitudinal mode, T for the in-plane transverse mode, and T′ for the out-of-plane transverse mode. Please note that 'Mode' represents the most sensitive mode in a specific scattering geometry and a field direction.

Extended Data Table 2 | Comparison to previous reports of hidden order in Sr_2IrO_4

	Observation	Interpretation	Inconsistency with our data
SHG	• Breaking of inversion and rotational symmetries at $T_{HO} \sim 243$ K in undoped Sr_2IrO_4, and at $T_{HO} \sim 210$ K for 4 % Rh-doped sample.	• Symmetry consistent with magneto-electric loop current. • Reinterpreted as due to surface magnetization induced electric-dipole SHG process based on additional experiments in magnetic field (for undoped sample).	• T_{HO} and T_C different by ~ 20 K (for undoped sample). • Inconsistent with PND and TM (ferroic stacking along c-axis).
PND	• Spin-flip scattering at $\mathbf{Q} = (1, 1, 2)$ setting in at $T_{HO} \sim 240 \pm 30$ K for both parent and 7 % Rh-doped samples.	• Symmetry consistent with magneto-electric loop current (but of different type from the one suggested by SHG).	• **Q** vector different from our x-ray data; CD is observed at (0 0 odd). • $T_{HO} \sim 240$ K is much lower than our $T_C \sim 263$ K. • Our magneto-optical Kerr effect data rules out any time-reversal breaking order.
TM	• Broken C_4 symmetry at $T_{HO} \sim 270$ K for the parent compound.	• Nematic phase transition (but distinct from nematic orders reported in other systems, which have even parity).	• Consistent with our data. • $T_{HO} \sim T_C$
ER	• Absence of divergent behavior in the nematic susceptibility, which suggests odd parity.	• Together with the magnetic torque data, the hidden order is suggested to be a loop current order.	• The data is available only for Rh-doped samples.

The SN order discovered in our work is symmetry distinct from that of a loop current (LC) order, originally suggested to account for the pseudogap in cuprates[46] and much discussed recently in Sr_2IrO_4 as a possible origin of the hidden order. Below, we have summarized the previous reports based on second harmonic generation (SHG)[40,47], polarized neutron diffraction (PND)[41], torque magnetometry (TM)[42], and elastoresistance (ER)[42] measurements, and compared them with our results.